On the breakup of fluid rivulets

Javier A. Diez,[1] Alejandro G. González,[1] and Lou Kondic[2]
[1]*Instituto de Física Arroyo Seco, Universidad Nacional del Centro de la Provincia de Buenos Aires, Pinto 399, Tandil 7000, Argentina*
[2]*Department of Mathematical Sciences, Center for Applied Mathematics and Statistics, New Jersey Institute of Technology, Newark, New Jersey 07102, USA*

(Received 8 April 2009; accepted 3 August 2009; published online 31 August 2009)

We study the stability of rivulets on horizontal substrates. The implemented model includes the effects of capillarity, fluid-solid interaction, and gravity if appropriate, within the framework of the lubrication approximation. We find that the results compare favorably with those in literature, in the regime where previous analyses are valid. By isolating the effect of van der Waals interactions for nanoscale rivulets, and of gravity for macrosize rivulets, we are able to analyze the influence of these forces on the stability. We discuss in detail the scaling of the emerging wavelengths (distance between drops formed after the breakup process) with the rivulet cross-sectional area. Perhaps surprisingly, we uncover close connection between this scaling and the one for the breakup of a free-space fluid jet (Rayleigh–Plateau instability). Finally, we consider rivulets of finite length and find that the finite size effects are considerably different from the ones obtained previously for semi-infinite fluid films. © *2009 American Institute of Physics*. [DOI: 10.1063/1.3211248]

I. INTRODUCTION

The stability of thin films and rivulets is a subject of increasing importance and relevance. Numerous applications in the field of micro- and nanofluidics,[1,2] as well as templating or lithographic patterning and various types of coatings[3–5] warrant careful and detailed analysis of this subject. In addition, this problem provides significant mathematical and modeling challenges due to the presence of multiple spatial and temporal scales, as well as the need to incorporate microscale physics into a continuum fluid dynamical model. Thin films on the scales ranging from nano to macro have been extensively studied by means of experiments, simulations, and analysis.

Particularly interesting issues arise on the short scales, where the stability is influenced by the competition of the capillary forces with the ones resulting from liquid-solid interaction.[6–8] In all of these examples, the films are often unstable and break up, leading to the formation of dry spots. The instability has been found to be either driven by nucleation at defect sites which are not spatially correlated, or via spinodal type of instabilities resulting in a spatial correlation.[8,9] Interesting issues arise also during dewetting of laser-illuminated thin metal films where similar type of behavior is observed as for more commonly considered fluids.[8,10,11]

The analysis of the stability of thin rivulets has also been studied, although to a significantly lesser extent than that of thin films. The pioneering study of rivulet instability was done by Davis,[12] who considered a static rivulet on a horizontal substrate. His analysis is based on an energylike integral form of the Navier–Stokes equations linearized after perturbing the straight contact lines. This method yields a sufficient condition for stability in terms of the critical (marginal) wavenumber as a function of the equilibrium contact angle. Some years later, Sekimoto *et al.*[13] studied spatial perturbations of the rivulet steady state solution (with small slopes and including gravity) by using a variational principle that leads to a minimum of surface energy. The stability criterion for a given wavenumber of the perturbation is based on the appearance of spatially divergent solutions resulting from the implemented variational method.

Other authors considered the problem of the rivulet instability with additional effects. For instance, Young and Davis[14] studied the rivulet on an inclined plane where gravity produces an axial flow, and Wilson *et al.*[15] are concerned with its viscoplasticity on a slowly varying substrate. Duinveld[16] considered its stability in relation with ink-jet printing lines. Brochard-Wyart and Redon[7] performed a stability study based on the analysis of the free energy of the rivulet. The problem of the rivulet on a plane substrate was also treated as a particular case of flow in a wedge by Langbein,[17] Roy and Schwartz,[18] and Yang and Homsy.[19] All of these works, with exception of Sekimoto *et al.*,[13] considered a rivulet cross section as an arc of a circle with specified contact angle, therefore ignoring the effect of gravity.

The stability of rivulets has also been considered in the presence of axial flow. In those cases, this flow has been found to have a stabilizing effect.[20] Moreover, not only fluid but also solid rivulets have been considered. For instance, McCallum *et al.*[21] followed a similar procedure as Davis[12] to account for the stability of a solid rivulet which evolves by surface diffusion.[22]

One interesting question is the relation between the stability of a (infinite-length) rivulet and that of a free-space jet (the Rayleigh–Plateau problem). One may rightfully wonder why there should be a connection between these two problems since breakup of a rivulet is governed by the balance between the forces due to viscosity, capillarity, and liquid-solid interaction (and possibly gravity). This contrasts with the Rayleigh–Plateau problem, where liquid-solid interaction is absent, and viscous effects do not influence the main features of instability development, such as critical wavelength.

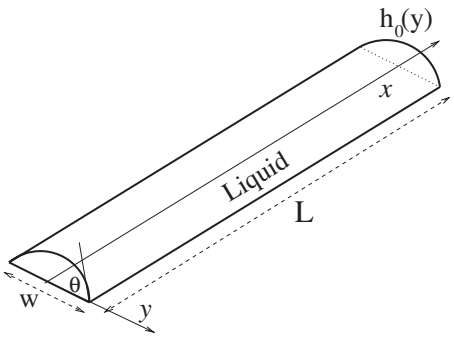

FIG. 1. Schematic of a fluid rivulet on a horizontal substrate.

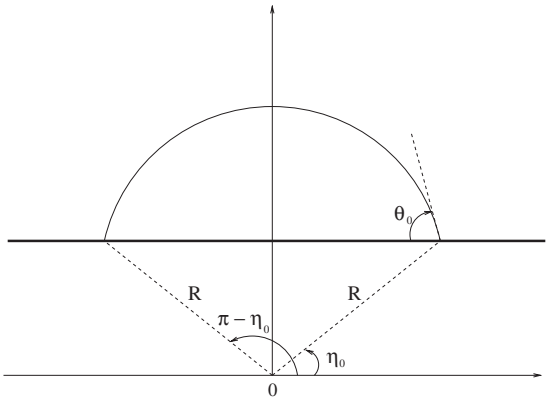

FIG. 2. Scheme of the circular cross section and angles definition.

However, the geometric similarity of the two configurations have inspired some comparisons in literature. For example, Park *et al.*[23] studied experimentally the rupture of polymer rivulets of micrometric width and found fairly good agreement with the Rayleigh prediction, but did not discuss the motivation for this comparison. Kondic *et al.*[11] considered computationally and experimentally the breakup of nanometric laser-irradiated metal films and also found excellent agreement with the Rayleigh–Plateau prediction. The question is how general these results are and to which degree can the two problems, breakup of a fluid rivulet and of a free-standing fluid jet, be correlated.

In this paper we consider the stability of rivulets on horizontal substrates within the framework of lubrication model (see Fig. 1). Although main motivation of this work is to analyze the effect of finite rivulet length on stability, we find that it is necessary to review the problem of the infinite-length rivulet first. This review is appropriate on its own right since detailed comparison of the existing results is lacking. Therefore, we begin this paper by discussing extensively previous work in the field (Sec. II). Then, in Sec. III we carry out linear stability analysis (LSA) of an infinite-length rivulet including gravitational effects, as well as partial wetting effects using disjoining pressure model. We analyze, in particular, the influence of van der Waals (vdW) forces and gravity on the stability, and discuss the regimes where earlier results do or do not describe accurately the rivulet stability. Numerical simulations of the fully nonlinear problem follow in Sec. V, where we also study the effect of finite length of a rivulet on instability. Due to the relevance of rivulet instability in the applications at a variety of scales, we consider separately the stability of macro- and nanosized rivulets. Macroscale rivulets of thickness comparable to capillary length are considered in Secs. IV and V, both with and without gravitational effects. The stability of nanorivulets is discussed in Sec. VI. Some additional problems are outlined in Sec. VII.

II. STABILITY ANALYSIS OF INFINITE-LENGTH RIVULETS: REVISITED

As mentioned in Sec. I, the stability of an infinite fluid rivulet on a solid surface has been investigated by a number of researchers.[7,12,13,17–19] Since these works are based on different theoretical approaches, and have never been compared against each other, we devote this section to their comparison. In the rest of the paper, we will use this comparison to also relate our own results to the existing ones. One important point is that some of the referenced works use the lubrication approach and other ones do not. Therefore, the following discussion of those results allows us to analyze the validity of the lubrication approximation in configurations characterized by large contact angles.

We first concentrate on the seminal paper by Davis,[12] where a linearized hydrodynamic theory for static rivulets without gravity effects was developed. A rivulet of circular cross section with given (fixed) radius R, density ρ, surface tension γ, and contact angle θ_0 is considered in that paper. For perturbations with axial wavenumber k ($=2\pi/\lambda$, λ being the wavelength) and growth rate σ, Davis obtained the energy balance equation

$$\sigma^2 E_k + \sigma E_v + I = 0, \tag{1}$$

where E_k is the kinetic energy, E_v is a generalized viscous dissipation, and I is the interfacial energy,

$$I = \int_{\theta_0}^{\pi-\theta_0} [(k^2-1)|\phi|^2 + |\phi_\theta|^2] d\theta - [\phi^* \phi_\theta]_{\theta_0}^{\pi-\theta_0}. \tag{2}$$

Here, ϕ is the interfacial normal speed for normal modes in units of $\sqrt{\gamma/\rho R}$ and * denotes complex conjugation. By examining the discriminant of Eq. (1), Davis found that a sufficient condition of stability is $I>0$. For *fixed contact angles*, the functional I satisfies the inequality,

$$I \geq [\zeta(\theta_0) + k^2 R^2 - 1] \int_{\theta_0}^{\pi-\theta_0} |\phi|^2 d\theta, \tag{3}$$

where $\zeta(\theta_0)$ is obtained by solving the following Euler–Lagrange equations:

$$\phi_{\eta\eta} + \zeta(\theta_0)\phi = 0, \tag{4}$$

$$\phi_\eta + \phi \cot \theta_0 = 0, \quad \eta = \eta_0, \tag{5}$$

$$\phi_\eta - \phi \cot \theta_0 = 0, \quad \eta = \pi - \eta_0, \tag{6}$$

and $\eta_0 = \pi/2 - \theta_0$ (see Fig. 2). Thus, his linearized stability condition is

$$k^2 R^2 > k_c^2 R^2 = 1 - \zeta(\theta_0), \tag{7}$$

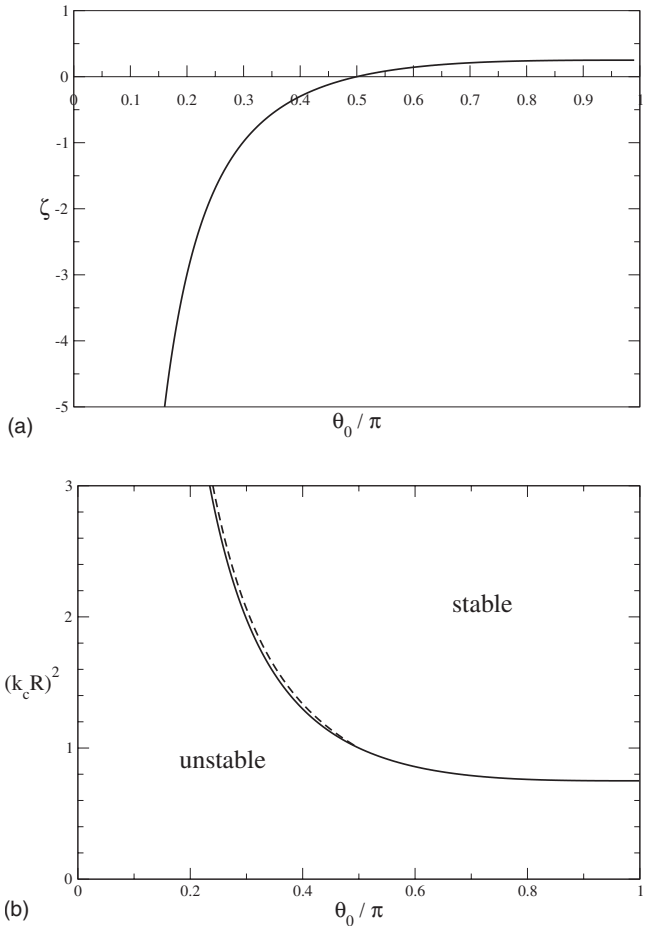

FIG. 3. Comparison of the results in Refs. 12 and 19. (a) Solution of Eqs. (9) and (10) for real s ($\zeta>0$) and imaginary s ($\zeta<0$). (b) Stability diagram: The solid line corresponds to Ref. 12, our Eq. (7), and the dashed line to Ref. 19, our Eq. (15).

where k_c is the critical wavenumber. *Fixed contact line* problem was also considered in Ref. 12 but we do not discuss that configuration in any detail here.

We proceed to find $\zeta(\theta_0)$ by writing the solution of Eq. (4) in the form

$$\phi = A\cos s\eta + B\sin s\eta, \tag{8}$$

with $s^2=\zeta$, and A and B as real constants. Thus, we see that ζ can be physically understood as the wavenumber in the azimuthal direction, η, and then, the marginal condition in Eq. (7) corresponds to the total (axial plus azimuthal) dimensionless wavenumber equal to unity.

By applying the boundary conditions given by Eqs. (5) and (6), we obtain a linear system of equations for A and B. A nontrivial solution is found if the conditions specified by Eqs. (9) and (10) that follow are satisfied. For $\zeta>0$, we have

$$s_r \tan\theta_0 \tan(s_r\theta_0) = -1, \tag{9}$$

where $s=s_r\in\Re$. For $\zeta<0$, we have $s=is_i$ with $s_i\in\Re$, given by

$$s_i \tan\theta_0 \tanh(s_i\theta_0) = 1. \tag{10}$$

The solutions of Eqs. (9) and (10) yield $\zeta(\theta_0)$. This result is shown in Fig. 3(a), which is coincident with Fig. 4 in Ref. 12. The line dividing the regions of stability/instability given by Eq. (7) is shown in Fig. 3(b) (see Fig. 7 in Ref. 12).

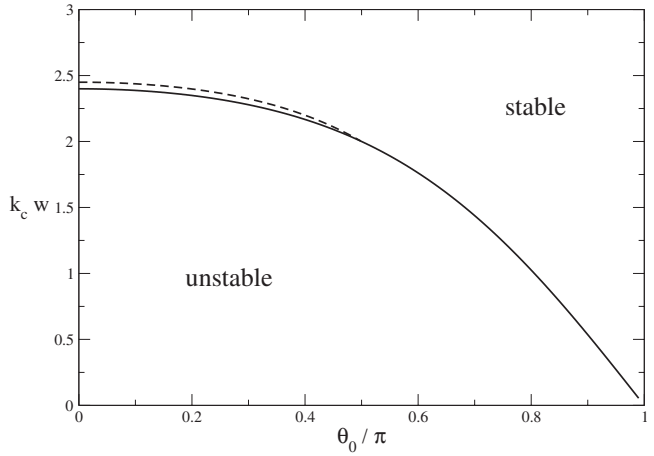

FIG. 4. Stability diagram in terms of rivulet width, w: The solid line corresponds to Davis (Ref. 12) theory as in Fig. 3(b), now plotted in terms of the rivulet width, w. This curve is identical to Fig. 5 in Ref. 18. The dashed line is specified by Eq. (15) of this paper; see Ref. 19.

Langbein[17] and Roy and Schwartz[18] studied the flow in a V-shaped surface so that our plane substrate is a particular case of their more general study. First, we note that Eq. (9) is equivalent to Eq. (25) in Ref. 17 for a plane substrate, showing that Davis' theory is recovered from Ref. 17. Also, we observe that Eqs. (9) and (10) are equivalent to Eqs. (3.15) and (3.16) in Ref. 18 [see also Eq. (7)] when applied to a plane surface. Therefore, the general treatment carried out in Ref. 18 is equivalent to that by Davis,[12] although that was apparently not clear at the time of publication. The main difficulty when comparing these three approaches is the choice of different variables to describe the marginal stability criterion. For example, instead of using R to define the critical wavenumber as in Ref. 12, k_c is in Ref. 18 given in terms of the rivulet width

$$w = 2R\sin\theta_0. \tag{11}$$

Figure 4 shows the stability diagram resulting from Ref. 12, now plotted in terms of w. This curve is identical to that in Fig. 5 in Ref. 18, thus showing the equivalence between both treatments. The dashed line in that figure corresponds to the approach in Ref. 19, which is discussed below.

A perhaps counterintuitive feature of the stability curve in Fig. 3(b) is that for $\theta_0\to 0$ the rivulet becomes unstable for all wavenumbers. This result seems to suggest that a fluid characterized by better wetting properties is more unstable. However, since R is fixed (and contact angle independent), the rivulet effectively disappears in the limit $\theta_0\to 0$, resolving the apparent contradiction.[24]

The limit $\theta_0\to\pi$ corresponds to a completely cylindrical rivulet with the contact line along a generatrix. Thus, one is tempted to compare the results with those of the Rayleigh–Plateau stability for a freestanding jet. It is shown by Davis[12] that his approach is consistent with Rayleigh's result, namely, $k_cR=1$, only when there is no contact line contribution to the energy balance. However, if one considers $\theta_0=\pi$, *and* assumes "fixed contact line," then one instead finds in-

creased stability, $k_cR=\sqrt{3/4}$.[12] Figure 3(b) shows that the same stability criterion is recovered if in the "fixed contact angle" approach one considers $\theta_0=\pi$ and *keeps* the contact line contribution in the energy balance, as discussed also in Ref. 21 for a solid rivulet. We will discuss the comparisons with the Rayleigh–Plateau theory for general θ_0 in more detail later on.

Similar to Refs. 17 and 18, Yang and Homsy[19] also considered a V-shaped surface. New ingredients are the inclusion of the axial curvature in the determination of the pressure field,[25] as well as the use of a mass conservation equation for the axial flow.[26] Lubrication approximation is used to determine the internal pressure. As in Ref. 12, the shape of the rivulet's cross section is that of an arc of a circle. A time-dependent equation for the rivulet width is obtained, and the stability analysis is performed by perturbing contact lines' positions. The corresponding dispersion relation for the growth rate, σ, results in

$$\omega(q) = q^2 - q^4, \tag{12}$$

where $\omega=\sigma t_0$ and $q=kz_0$ are dimensionless growth rate and wavenumber, respectively. The scales depend on θ_0 as

$$t_0 = Q_0^*(\theta_0)\frac{\mu R}{\gamma}\frac{(2\theta_0 - \sin 2\theta_0)(1+\sin^2\theta_0 - \theta_0\cot\theta_0)}{2\sin^4\theta_0}, \tag{13}$$

$$z_0 = R\sqrt{\frac{1+\sin^2\theta_0 - \theta_0\cot\theta_0}{2}}. \tag{14}$$

Here, $Q_0^*(\theta_0)$ is a dimensionless geometric function proportional to the volumetric flow. From Eq. (12), we have that marginal instability corresponds to $q_c=1$. Thus, the critical (dimensional) wavenumber, k_c, is given by

$$k_c^2R^2 = 2[1+\sin^2\theta_0 - \theta_0\cot\theta_0]^{-1}. \tag{15}$$

Figure 3(b) shows this result (dashed line). The agreement with Ref. 12 for $\theta_0<\pi/2$ is remarkable, recalling in particular that the lubrication approximation was used in Ref. 19. This result encourages us to expect that our own stability analysis, which is also based on lubrication approximation, will hold at large contact angles.

As mentioned above, Figs. 3(b) and 4 correspond to a rivulet of circular cross section with fixed radius of curvature, R. Therefore, the area, A, of the cross section varies with the contact angle, θ_0, as $A=R^2\mathcal{A}(\theta_0)$, where

$$\mathcal{A}(\theta_0) = \left(\theta_0 - \frac{\sin 2\theta_0}{2}\right). \tag{16}$$

Thus, we see that $A\to 0$ as $\theta_0\to 0$ for given R. However, one would like to consider the influence of contact angle on the stability without having to deal with vanishing rivulets for complete wetting. In order to do so, it is useful to define the dimensionless quantity

$$\Phi = k_cA^{1/2} \tag{17}$$

instead of k_cR as used in Fig. 3(b). Therefore, now we consider the case where A is fixed and, consequently, $R\to\infty$ as $\theta_0\to 0$. In terms of this combination, the stability boundary

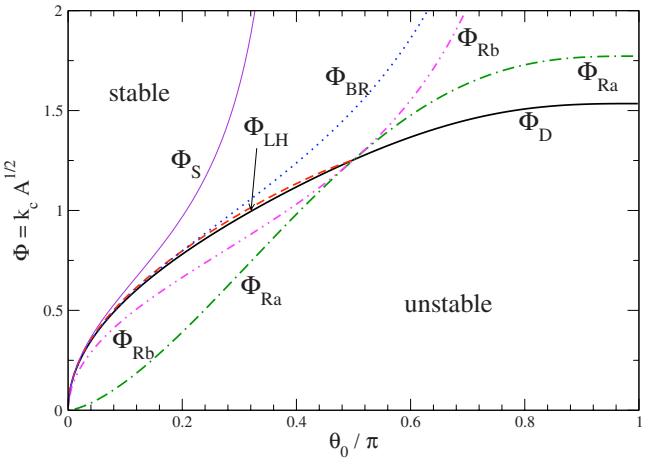

FIG. 5. (Color online) Stability diagram for *fixed area*, A. Different approaches are compared: Φ_D from Davis (Ref. 12) [(black) thick solid line], (b) Φ_{LH} from Ref. 19 [(red) dashed line], (c) Φ_{BR} from Ref. 7 [(blue) dotted line], and Rayleigh–Plateau instability of a fluid jet: Φ_{Ra} (green) dashed-dotted line for $R_{jet}=R$, and Φ_{Rb} (magenta) dashed-double dotted line for $R_{jet}=w/2$. Φ_S is the approach with gravity from Ref. 13 [(violet) thin solid line] for very small area, $A=0.001a^2$.

from Davis' theory[12] [see Eq. (7)] can be written as

$$\Phi_D = \sqrt{\mathcal{A}(\theta_0)[1-\zeta(\theta_0)]}. \tag{18}$$

Figure 5 shows this result, as well as other relevant ones discussed below. From Eq. (18) [(black) solid line in Fig. 5] we see that stability is recovered for complete wetting, $\theta_0\to 0$. The limit $\theta_0\to\pi$ yields $\Phi_D=\sqrt{3\pi/4}$, as discussed above.

The corresponding Φ for Ref. 19 approach is obtained by eliminating R from Eqs. (15) and (16),

$$\Phi_{LH} = \sqrt{2\mathcal{A}(\theta_0)[1+\sin^2\theta_0 - \theta_0\cot\theta_0]^{-1}}. \tag{19}$$

This result is also shown in Fig. 5. We note in passing that for constant $\mathcal{A}$, the maximum growth rate, σ_m, is given by

$$\sigma_m^{LH} = \frac{1}{4t_0}. \tag{20}$$

This expression will be used later for comparison with our own and other authors' results.

We proceed with discussing few more relevant results from literature. Brochard-Wyart and Redon[7] studied the relaxation time of sinusoidally distorted contact lines of a rivulet with circular cross section. For the viscous regime, they found the following dispersion relation:

$$\sigma = \frac{\gamma}{3\mu}\frac{\theta^3}{wF}\Psi(\xi), \tag{21}$$

where $\xi=kw$, and F is a logarithmic factor of order ten reflecting the singularity at the contact line.[27] $\Psi(\xi)$ is given by

$$\Psi(\xi) = \frac{2+\xi\tanh(\xi/2)}{1+4/\xi^2}. \tag{22}$$

From this result, one finds $\xi_c=k_cw\approx 2.4$ for $F=10$, in agreement with Ref. 18 for $\theta=0$ (see Fig. 4). This is expected

since the approach in Ref. 7 is valid for small θ. The stability boundary is given by

$$\Phi_{\mathrm{BR}} = \frac{\xi_c}{2}\frac{\mathcal{A}(\theta_0)^{1/2}}{\sin\theta_0}. \tag{23}$$

For small θ_0, there is an excellent agreement between Φ_{BR} and Φ_D, as shown in Fig. 5. For future reference, we also give the maximum growth rate

$$\sigma_m^{\mathrm{BR}} = \frac{\gamma}{\mu R}\frac{\theta^3}{6F\sin\theta}\Psi(\xi_m), \tag{24}$$

where $\xi_m = k_m w \approx 1.421$ and $\Psi(\xi_m) \approx 0.379$.

Next, we compare the results for the critical wavenumber with the one expected from the Rayleigh–Plateau instability of a freestanding fluid jet. For that problem, one expects a breakup to occur for wavelengths longer than $\lambda_c = 2\pi R_{\mathrm{jet}}$, where R_{jet} is the jet radius. There are at least two reasonable choices of an equivalent R_{jet} in our problem. One can assume that (a) R_{jet} is analogous to the radius of the circle that (best) describes the cross section, $R_{\mathrm{jet}} = R$, as used in Ref. 12, or (b) R_{jet} corresponds to the rivulet half width, $R_{\mathrm{jet}} = w/2 = R\sin\theta_0$, as considered in, e.g., Ref. 23. Then, using Eq. (16), we find that the corresponding Φ's for the equivalent Rayleigh–Plateau problem are

$$\Phi_{Ra} = \frac{\mathcal{A}(\theta_0)^{1/2}}{\sin\theta_0}, \quad R_{\mathrm{jet}} = R, \tag{25}$$

$$\Phi_{Rb} = \mathcal{A}(\theta_0)^{1/2}, \quad R_{\mathrm{jet}} = w/2 = R\sin\theta_0, \tag{26}$$

which are shown in Fig. 5. Both options are equivalent for $\theta_0 = \pi/2$, where they coincide with Φ_D. While the behavior of option (a) is similar to that of Φ_D for $\theta_0 \to \pi$, it strongly differs from it for $\theta_0 < \pi/2$. On the other hand, option (b) is closer to Φ_D in this range of contact angles. Since in this work we are concerned only with $\theta_0 < \pi/2$, we use option (b) in further comparisons.

Finally, we discuss the results by Sekimoto *et al.*[13] which included gravity effects. In this work, the authors consider the rivulet steady state solution with small slopes. By using a variational principle they obtain a stability criterion from the eigenvalue spectra of spatial perturbations. In this approach, unstable modes are characterized by spatially divergent solutions. This is somewhat different to the studies discussed previously, where stability is related to the temporal growth of the perturbations.

The criterion for stability of the varicose mode can be derived from their Eq. (4.21) as

$$\sqrt{a^2 + k_c^2}\tanh\left(\frac{w}{2a}\sqrt{a^2 + k_c^2}\right)\tanh\left(\frac{w}{2a}\right) = 1, \tag{27}$$

where $a = \sqrt{\gamma/\rho g}$ is the capillary length, and w now refers to the rivulet width with gravity [i.e., not given by Eq. (11)]. In this case, the conditions of zero thickness and prescribed contact angle apply at the contact line, and, consequently, w is determined by (see, e.g., Appendix B in Ref. 9)

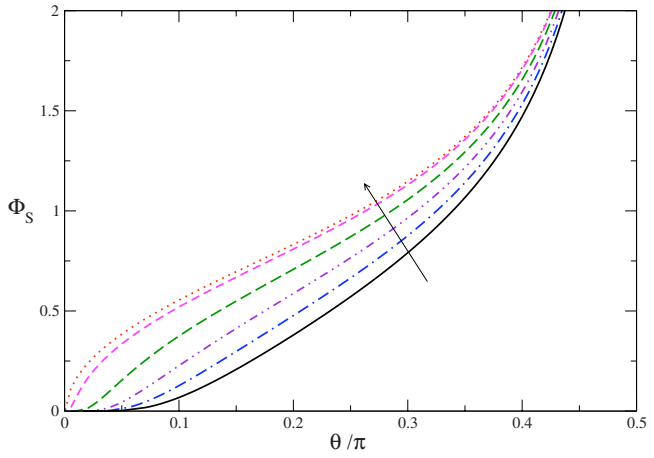

FIG. 6. (Color online) Stability diagram with gravity effects from Ref. 13 for $\tilde{A} = A/a^2 = 2.0$ [(black) solid line], 1.5 [(blue) dotted-dashed line], 1.0 [(violet) double dotted-dashed line], 0.5 [(green) long-dashed line], 0.1 [(magenta) short-dashed line], and 0.01 [(red) dotted line]. The arrow indicates the direction of decreasing $\tilde{A}$.

$$w = a\left(2 + \frac{A}{a^2\tan\theta}\right)\tanh\left(\frac{w}{2a}\right). \tag{28}$$

Thus, Eqs. (27) and (28) allow to obtain $k_c(w)$ and $w(A,\theta)$, respectively. Here, due to the presence of gravity, the corresponding combination Φ_S is not independent of A since the shape of the cross section now changes with the area—it becomes flatter as A increases. Figure 6 shows Φ_S versus θ for different A's. Note that gravity strongly affects the value of k_c for small θ, by decreasing k_c as A increases. We will consider this effect below when vdW forces are included. Figure 5 shows that for very small A, the marginal stability line is similar to Φ_D. This follows from the fact that an arc of a circle becomes a good approximation for the cross section when gravity effects are weak.

To conclude, we find that existing approaches to stability of infinite-length rivulets lead to results which are consistent in their respective ranges of validity. However, one needs to be careful when using these results due to different scalings of the problem. Also, one has to bear in mind that there is not a single way to analyze the stability in terms of the freestanding fluid jet. We will find that proper understanding of the existing results is crucial when developing the following model, which includes gravitational effects as well as intermolecular forces.

III. LINEAR STABILITY ANALYSIS OF AN INFINITE RIVULET

In this section we formulate the model that we use to analyze stability of rivulets. One important difference compared to earlier works is that we include vdW liquid-solid interaction directly into the formulation. The vdW potential naturally introduces the apparent contact angle, θ, defined by the requirement that the slope of the free surface far away from the contact line is equal to $\tan\theta$ (see e.g., Fig. 30 in Ref. 9). For the purpose of comparison with previously discussed results, we typically choose $\theta \approx \theta_0$, where θ_0 is the

imposed contact angle of an arc of a circle.[12,17,19] The precise relation between θ and θ_0 is discussed in detail later.

The inclusion of vdW forces is based on the conjoining/disjoining pressure model (see, e.g., Ref. 9 and the references therein). This additional contribution leads to variable curvature along the rivulet boundary, and correspondingly the rivulet cross section can no longer be described as an arc of a circle, but has to be determined from the governing equations, discussed next. The departure from the circular shape in the contact region due to the introduction of these forces may be substantial in the case of rivulets of microscopic and nanoscopic size. For macroscopic rivulets, the lack of circularity mainly appears in the bulk region due to gravity effects, which flatten the profile.

A. Base solution

The mathematical model is very similar to the one used when considering thin films with vdW contribution.[9] For completeness, here we give the main ideas. We refer the reader to Ref. 9 also regarding the use of the lubrication approximation for relatively large contact angles. In the present framework, this approach is further justified by the excellent comparison between the previous works using[19] or not[12] lubrication approximation.

The governing equation for the fluid thickness, $h=h(x,y,t)$, is

$$3\mu\frac{\partial h}{\partial t}+\gamma\nabla(h^3\nabla\nabla^2 h)+\nabla[h^3\nabla\Pi(h)]-\rho g\nabla(h^3\nabla h)=0, \tag{29}$$

where μ is the viscosity and g is the gravity. Here, the first term stands for viscous dissipation and the other three terms account for the driving forces, which are surface tension, vdW, and gravity force, respectively. The disjoining pressure model here employed is

$$\Pi(h)=\kappa f(h)=\kappa\left[\left(\frac{h_*}{h}\right)^n-\left(\frac{h_*}{h}\right)^m\right], \tag{30}$$

which introduces κ (proportional to the Hamaker constant) and the exponents $n>m>1$ (note that $f(h)$ is a dimensionless function). The first term represents liquid-solid repulsion, while the second term is attractive, leading to a stable film thickness $h=h_*$. Within this model, $\kappa=S/(Mh_*)$, where S is the spreading parameter and $M=(n-m)/[(m-1)(n-1)]$ (see Ref. 9). The spreading parameter can be related to the apparent contact angle θ via the Young–Laplace condition, $S=\gamma(1-\cos\theta)$.

We take the x-axis along the rivulet, and the y-axis in the transverse direction. By defining the dimensionless variables $\tilde{h}=h/h_s$, $\tilde{x}=x/x_s$, $\tilde{y}=y/x_s$, and $\tilde{t}=t/t_s$, with

$$t_s=\frac{3\mu}{\gamma}\frac{x_s^4}{h_s^3},$$

Eq. (29) becomes

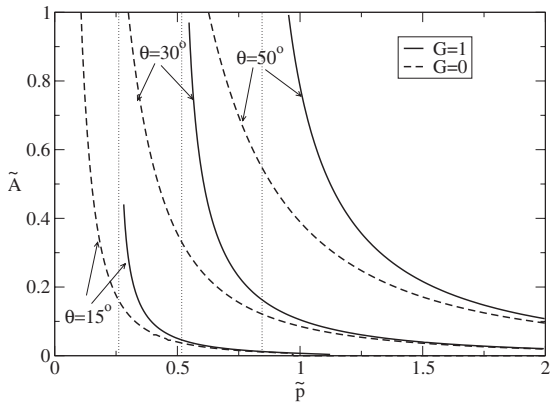

FIG. 7. Relationship between the pressure, $\tilde{p}$, Eq. (34) and the corresponding area, $\tilde{A}$, of the rivulet cross section for three different contact angles, θ. For $G=1$ (gravity included, solid lines) $\tilde{p}$ must be greater than a critical values, $\tilde{p}_c$, shown by dotted lines. For $G=0$ (no gravity, dashed lines), there is no lower limit for $\tilde{p}$.

$$\frac{\partial\tilde{h}}{\partial\tilde{t}}+\tilde{\nabla}\cdot(\tilde{h}^3\tilde{\nabla}\tilde{\nabla}^2\tilde{h})+K\tilde{\nabla}\cdot[\tilde{h}^3 f'\tilde{\nabla}\tilde{h}]-D\tilde{\nabla}\cdot(\tilde{h}^3\tilde{\nabla}\tilde{h})=0, \tag{31}$$

where $f'=df/d\tilde{h}$. The dimensionless constants are given by

$$D=G\frac{x_s^2}{a^2},\quad K=\frac{\kappa}{\gamma}\frac{x_s^2}{h_s}. \tag{32}$$

We use $G=1$ when gravity effects are considered and $G=0$ when they are neglected.

We first concentrate on the $\tilde{x}$-independent solution, $\tilde{h}(\tilde{y},\tilde{t})$, so that Eq. (31) reduces to

$$\frac{\partial\tilde{h}}{\partial\tilde{t}}+\frac{\partial}{\partial\tilde{y}}\left[\tilde{h}^3\left(\frac{\partial^3\tilde{h}}{\partial\tilde{y}^3}+Kf'\frac{\partial\tilde{h}}{\partial\tilde{y}}-G\frac{\partial\tilde{h}}{\partial\tilde{y}}\right)\right]=0. \tag{33}$$

We consider now $\partial\tilde{h}/\partial\tilde{t}=0$. After integrating twice the resulting equation and using the boundary conditions $\tilde{h}_0'''=\tilde{h}_0'=0$ at $\tilde{y}=\pm\infty$, where the primes stand for $\tilde{y}$-derivatives, we obtain

$$\tilde{h}_0''+Kf(\tilde{h}_0)-G\tilde{h}_0+\tilde{p}=0, \tag{34}$$

where the constant $\tilde{p}>0$ is the equilibrium pressure[28,29] within the fluid (in units of $\gamma h_s/x_s^2$). An analysis[9,28,30] of the solutions of Eq. (34) shows that there is a range of pressures $\tilde{p}_c<\tilde{p}<\tilde{p}^*$ for which there exists bounded solution, such as $\tilde{h}_{0,\min}<\tilde{h}_0(\tilde{y})<\tilde{h}_{0,\max}=\tan\theta$. Within this range, the value of $\tilde{p}$ is related to the cross section area,

$$\tilde{A}=2\int_0^\infty(\tilde{h}_0(\tilde{y})-\tilde{h}_{0,\min})d\tilde{y}, \tag{35}$$

where $\tilde{h}_{0,\min}$ corresponds to the so-called precursor film thickness and it is found as discussed in Ref. 9. A first estimate of its value is given by $\tilde{h}_{0,\min}\approx\tilde{h}_*+\tilde{p}\tilde{h}_*/K(n-m)$.[9,28] Typically, the difference between $\tilde{h}_{0,\min}$ and $\tilde{h}_*$ is at most few percent [see, e.g., Fig. 31(a) in Ref. 9].

Figure 7 shows the relationship between $\tilde{p}$ and the corresponding area, $\tilde{A}$, with $(G=1)$ and without $(G=0)$ gravity

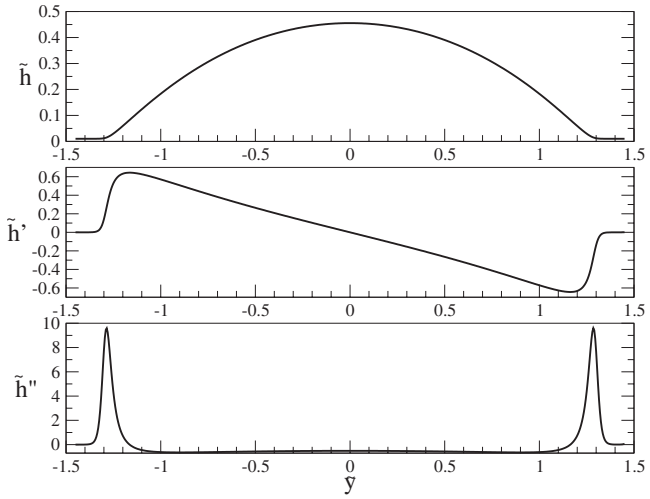

FIG. 8. Cross section of the rivulet for $\tilde{p}=1$ and $G=1$ ($\tilde{A}=0.763$). Here $n=3$, $m=2$, $\theta=50°$, and $\tilde{h}_*=0.01$.

[a typical profile of $h_0(x)$ is shown in Fig. 8(a)]. With gravity, $\tilde{p}$ has to be larger than a certain limit, $\tilde{p}_c$, and, consequently, the maximum drop thickness is bounded. The solution of Eq. (34) is studied in detail in Appendix B of Ref. 9.

B. Perturbations and the eigenvalue problem

In order to perform LSA of a rivulet, we perturb the base profile discussed above, $\tilde{h}_0(\tilde{y})$, by longitudinal modes in the $\tilde{x}$ direction as follows:

$$\tilde{h}(\tilde{x},\tilde{y},\tilde{t}) = \tilde{h}_0(\tilde{y}) + \epsilon \tilde{g}(\tilde{y})\exp(\tilde{\sigma}\tilde{t} + i\tilde{k}\tilde{x}), \tag{36}$$

where ϵ is a small parameter, $\tilde{g}(\tilde{y})$ is the amplitude, and $\tilde{k}=2\pi/\tilde{\lambda}$ is the (dimensionless) wavenumber, with $\tilde{\lambda}$ being the wavelength.

By replacing Eq. (36) into Eq. (33), we obtain to $O(\epsilon)$ the following eigenvalue problem:

$$\mathcal{L}\tilde{g} = -\tilde{\sigma}\tilde{g},$$

where $\mathcal{L}$ is the linear operator defined by

$$\mathcal{L}g = c_4(\tilde{y})\tilde{g}_{\tilde{y}\tilde{y}\tilde{y}\tilde{y}} + c_3(\tilde{y})\tilde{g}_{\tilde{y}\tilde{y}\tilde{y}} + c_2(\tilde{y})\tilde{g}_{\tilde{y}\tilde{y}} + c_1(\tilde{y})\tilde{g}_{\tilde{y}} + c_0(\tilde{y})\tilde{g}. \tag{37}$$

Here, the coefficients $c_i(\tilde{y})$ $(i=0,\ldots,4)$ are defined by

$$c_4(\tilde{y}) = \tilde{h}_0^3,$$

$$c_3(\tilde{y}) = 3\tilde{h}_0^2\tilde{h}_0', \tag{38}$$

$$c_2(\tilde{y}) = -[G + 2\tilde{k}^2 - Kf'(\tilde{h}_0)]\tilde{h}_0^3,$$

$$c_1(\tilde{y}) = -\tilde{h}_0^2\{3[G + \tilde{k}^2 - Kf'(\tilde{h}_0)] - 2\tilde{h}_0 Kf''(\tilde{h}_0)\}\tilde{h}_0', \tag{39}$$

$$c_0(\tilde{y}) = c_{0,2}\tilde{h}_0^2 + c_{0,3}\tilde{h}_0^3 + c_{0,4}\tilde{h}_0^4,$$

and $c_{0,j}$ $(j=2,3,4)$ are given by

$$c_{0,2}(\tilde{y}) = 3\tilde{h}_0'^2 Kf''(\tilde{h}_0),$$

$$c_{0,3}(\tilde{y}) = \tilde{k}^2[G + \tilde{k}^2 - Kf'(\tilde{h}_0)] - Kf''(\tilde{h}_0)[\tilde{p} + Kf(\tilde{h}_0)] + \tilde{h}_0'^2 Kf'''(\tilde{h}_0), \tag{40}$$

$$c_{0,4}(\tilde{y}) = GKf''(\tilde{h}_0).$$

Since the stability of rivulets is relevant to physical problems on different scales, we consider separately the stability of macroscopic rivulets (Sec. IV, where the effect of gravity is also included) and of nanoscale rivulets (Sec. VI).

IV. LINEAR STABILITY ANALYSIS OF MACROSCOPIC RIVULETS

In this section we focus on rivulets of millimetric or submillimetric maximum thickness, h_{apex}. In particular, we analyze the effects of a noncircular cross section either due to the vdW forces or due to gravity. For these rivulets, it is convenient to choose capillary length, a, as the length scale for both horizontal and vertical directions,

$$x_s = h_s = a. \tag{41}$$

Thus, we have $G=1$ ($G=0$) if gravity effects are (not) considered, and $K=(1-\cos\theta)a/(Mh_*)$. We also choose a base set of parameters: $n=3$, $m=2$, $\theta=50°$, and $h_*=0.01a$, unless stated otherwise. Different choice of scales will be appropriate for microscopic rivulets discussed in Sec. VI.

A. Rivulets under zero gravity ($G=0$)

The profile of the rivulet (base solution) is obtained by integrating Eq. (34) using a fifth order Runge–Kutta method. The numerical integration is performed forward from $\tilde{h}_{0,\min}$, with $\tilde{h}_0'$ a small quantity (typically, 10^{-6}), until $\tilde{h}_0'$ becomes zero, indicating that the apex has been reached. The position of this local maximum is taken to define $\tilde{y}=0$. Since Eq. (34) is symmetric under reflections $(y\to -y)$, it is clear that the solution will be symmetric. Figure 8 shows a typical rivulet cross section (base solution) for a representative value of the pressure, $\tilde{p}=1$, and given values of n, m, θ, and $\tilde{h}_*$.

The eigenvalue problem is solved using EISPACK routines. The calculation yields N eigenfunctions and eigenvalues, where N is the number of points that discretize Eq. (37) (N is of the order of 3000), and we choose the even and odd modes with the highest absolute value of its eigenvalue. Thus, only two modes are selected, a varicose (symmetric) mode and a zigzag (antisymmetric) mode.[7,13] Figures 9 and 10 show the corresponding eigenvalues and eigenfunctions for few different pressure values. We see that the zigzag mode is characterized by a nonpositive growth rate for all $\tilde{k}$'s ($\tilde{\sigma}=0$ at $\tilde{k}=0$ for both modes), while the varicose mode shows an unstable $\tilde{k}$ range. The zero growth rate at $\tilde{k}=0$ (for both the varicose and zigzag modes) is a direct consequence of volume conservation. We note that as long as the precursor, where all derivatives vanish, is present, we do not find any effects of the domain size on the LSA results.

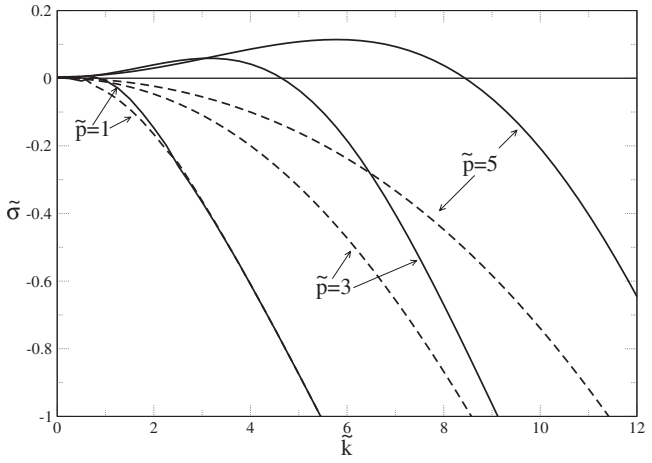

FIG. 9. Growth rate, $\tilde{\sigma}$, vs wavenumber, $\tilde{k}$, for $G=1$ with pressures $\tilde{p}=1,3,5$ ($\tilde{A}=0.763,0.041,0.012$). The varicose and zigzag dispersion curves are plotted as solid and dashed lines, respectively.

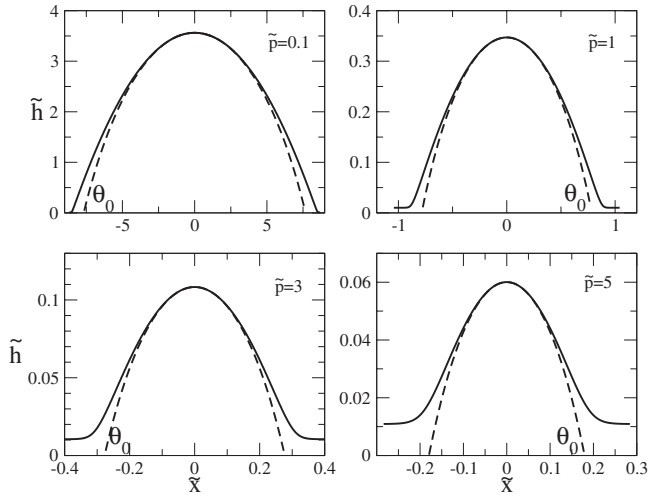

FIG. 11. Rivulet cross sections (solid lines) for $\theta=50°$ for $\tilde{p}=0.1,1,3,5$. The dashed lines are the corresponding osculating circles, with the contact angles given by $\theta_0=49.8°$, 47.7°, 42.7°, and 37.0°, respectively.

Due to translational invariance of the base solution, $\tilde{h}_0(\tilde{y})$, the varicose mode for $\tilde{k}=0$ is given by $\tilde{h}_0'(\tilde{y})$. We have verified that $\tilde{g}(\tilde{y})$ for $\tilde{k}=0$ and $\tilde{h}_0'(\tilde{y})$ (normalized to unity) are practically indistinguishable, confirming accuracy of the calculation.

In summary, we find a range of unstable wavenumbers only for varicose mode of perturbation. Clearly, larger pressures, corresponding to smaller rivulet cross sections, lead to more unstable rivulets. In what follows, we discuss the quantitative features of the agreement between the results obtained here (using LSA with vdW forces) and the results reported previously in literature (and revisited in Sec. II), characterized by a circular cross section and by ignoring vdW contribution to the pressure.

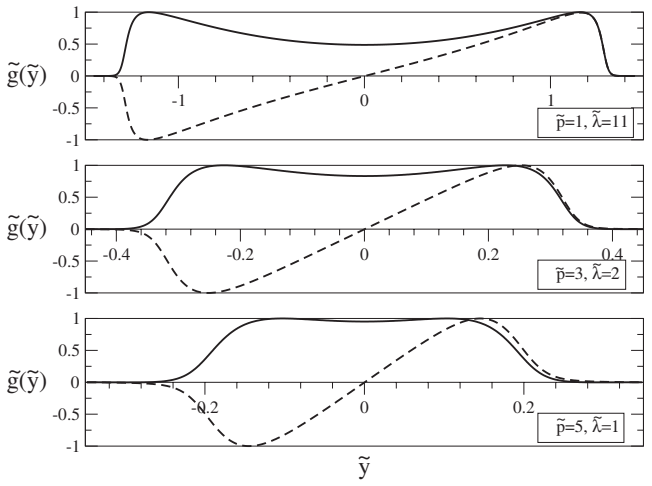

FIG. 10. Eigenfunctions, $\tilde{g}(\tilde{y})$, for the three cases in Fig. 9 at $\tilde{\lambda}=11,2,1$ close to the most unstable ones ($\tilde{\lambda}_m=11.22,1.92,1.09$, respectively). The varicose and zigzag eigenfunctions are plotted as solid and dashed lines, respectively.

1. Comparison of LSA with circular cross section theory

Now, we compare our LSA results with those reported in other works and discussed in Sec. II.[7,12,13,18,19] In those works, the authors do not include vdW forces to account for partial wetting, but instead consider a moving contact line whose instantaneous contact angle is fixed and equal to the static contact angle, θ_0. Since gravity is not considered in those studies, the cross section of the rivulet is approximately circular (due to the use of linearized curvature within lubrication approximation, the cross section is actually parabolic, but for simplicity we refer to it as circular). Then, a comparison requires the evaluation of the radius, $\tilde{R}=R/a$, of the osculating circle that best approximates the rivulet profile obtained by the present model. Figure 11 shows these osculating circles for different values of pressure $\tilde{p}$. We note that for smaller $\tilde{p}$'s, the height of the rivulet, $\tilde{h}_{\text{apex}}$, increases so that the ratio $r=\tilde{h}_*/\tilde{h}_{\text{apex}}$ decreases. Therefore, as $\tilde{p}\to 0$, and for fixed $\tilde{h}_*$, we expect to approach the description of a rivulet as an arc of a circle, and that the contact angle of the circle tends to that of a drop profile with vdW forces included, that is, $\theta_0\to\theta$. The same conclusion follows if $\tilde{p}$ is fixed, and $\tilde{h}_*\to 0$.

We first compare the critical wavenumber, $\tilde{k}_c$, as given by the present model, with earlier results.[12,19] Figure 12 shows the results of our LSA calculations for several values of $\tilde{p}, \theta$ and $\tilde{h}_*$ (symbols) together with the results from Ref. 12 (solid line) and Ref. 19 (dashed line). We see that the approach toward the above models with circular profiles is obtained as $\tilde{p}$ decreases (hollow symbols for $\theta=15°$, 30°, and 50°). If a thicker equilibrium thickness, $\tilde{h}_*$, is used, then a smaller value of $\tilde{p}$ is necessary to obtain a good agreement (see plus sign for $\theta=50°$, $\tilde{p}=0.5$, and $\tilde{h}_*=5\times 10^{-2}$). On the contrary, for smaller $\tilde{h}_*$, larger $\tilde{p}$ yields results close to that

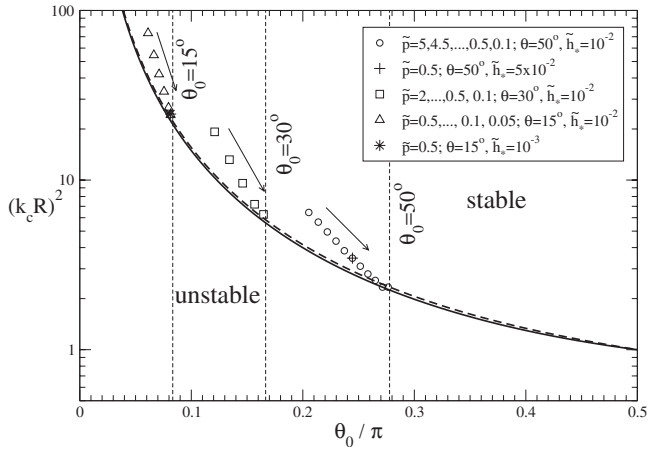

FIG. 12. Comparison of calculated critical wavenumber, $\tilde{k}_c$ multiplied by the radius of the osculating circle, $\tilde{R}$ (symbols) (note that $\tilde{k}_c\tilde{R}=k_cR$), with the results from Ref. 12 (solid line) and Ref. 19 (dashed line). The arrows indicate decreasing values of $\tilde{p}$ for the hollow symbols.

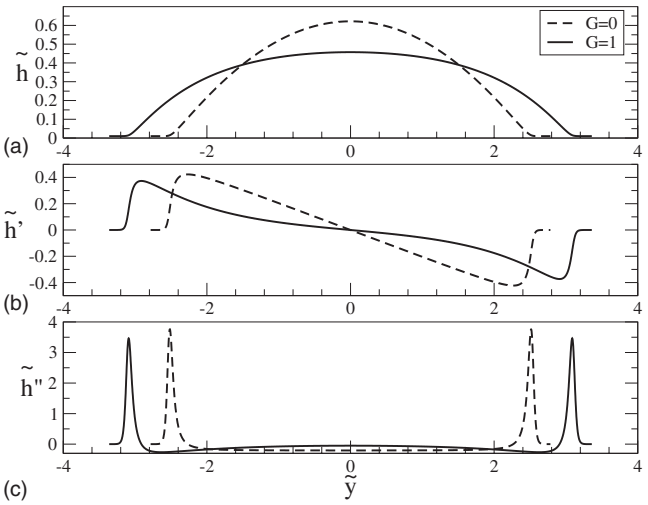

FIG. 14. Profiles of (a) thickness, (b) slope, and (c) curvature of a rivulet cross section for $\tilde{A}=2$ and $\theta=30°$ with ($G=1$, $\tilde{p}=0.520$) and without ($G=0$, $\tilde{p}=0.212$) gravity.

for smaller $\tilde{p}$ (see star sign for $\theta=15°$, $\tilde{p}=0.5$, and $\tilde{h}_*=10^{-3}$) Thus, smaller values of $\tilde{h}_*$ improve the agreement with circular cross section results.

Figure 13 shows the maximum growth rates obtained using the LSA developed here together with the results in Ref. 19, Eq. (20), and Ref. 7, Eq. (24). One difference between the two referenced approaches is that in Ref. 7 the energy dissipation rate is roughly approximated using the extreme values for $kw \ll 1$ and $kw \gg 1$, while in Ref. 19 the dissipation is treated exactly. We plot the dimensionless combinations $\Sigma_m^{\mathrm{LH}}=\sigma_m^{\mathrm{LH}}(R\mu/\gamma)$ (solid line) and $\Sigma_m^{\mathrm{BR}}=\sigma_m^{\mathrm{BR}}(R\mu/\gamma)$ (dashed line) versus θ_0, which should be compared to our variable $\Sigma=\tilde{\sigma}_m\tilde{R}/3$, where $\tilde{R}=R/a$. We observe that analogously to Fig. 12, decreasing $\tilde{p}$, for fixed θ and h_*, leads to Σ's which are closer to the curves (hollow symbols). Also here, larger h_* for a given $\tilde{p}$ leads to larger Σ (see plus sign for $\theta=50°$, $\tilde{p}=0.5$ and $\tilde{h}_*=5\times10^{-2}$) and smaller h_* yields Σ closer to the curves (star sign for $\theta=15°$, $\tilde{p}=0.5$, and $\tilde{h}_*=10^{-3}$). Although this comparison is not exhaustive, it shows that our LSA calculations compare well with earlier predictions.[7,19] Note that, in principle, one should not expect convergence of our calculations to existing theories, but only agreement in the orders of magnitude and tendencies of the predictions since the approaches are different.

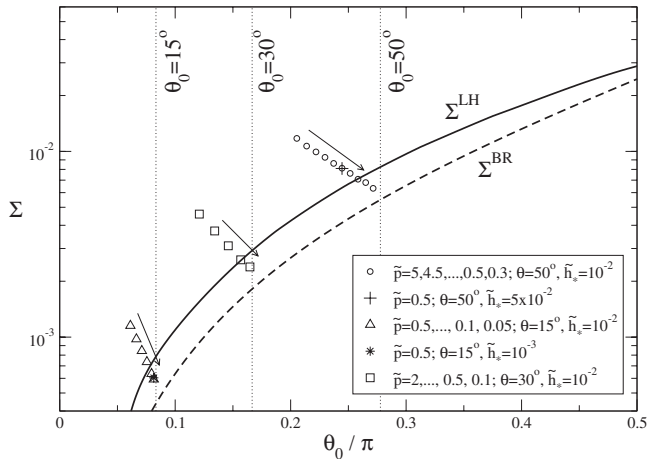

FIG. 13. Comparison of calculated maximum growth rates, Σ (symbols), with Ref. 19 (solid line) and Ref. 7 (dashed line), given here by Eqs. (20) and (24), respectively. The arrows indicate decreasing values of $\tilde{p}$ for the hollow symbols.

In summary, the results given here show that under the condition of zero gravity, the description of a rivulet cross section by a circle is a limiting case of the model with vdW forces for small $\tilde{p}$, i.e., for relatively thick rivulets. In this limit, the predictions of LSA carried out with vdW forces show good agreement with the previous results where fixed contact angle was imposed.[12,19]

B. Rivulets under gravity

Figure 14 shows the effect of gravity on a rivulet of relatively large cross section area (the corresponding p is close to p_c). Gravity flattens the thickness profile by reducing the maximum thickness of the rivulet, h_{apex}, and, consequently, increasing the rivulet width, w. Besides, both the bulk slope and the curvature are smaller for $G=1$ than for $G=0$. Therefore, gravity effects significantly modify the shape of a rivulet, and thus, a description of a rivulets' cross section as an arc of a circle is not appropriate for large $\tilde{A}$'s.

The effect of gravity on the dispersion relations resulting from the LSA is shown in Fig. 15. We see that gravity reduces both the maximum growth rate, $\tilde{\sigma}_m$, and the critical wavenumber, $\tilde{k}_c$. For large areas, only very long wavelengths are unstable.

Figure 16 shows the influence of gravity on the stability of a rivulet, and is the central figure of this section. Without gravity ($G=0$), the critical wavenumber reaches a constant value for large areas. This asymptotic behavior is well described by the result in Ref. 12 (horizontal dotted line in the figure). This trend of the results is the consequence of the fact that with gravity neglected, an arc of a circle is a good approximation of the rivulet cross section for large cross-

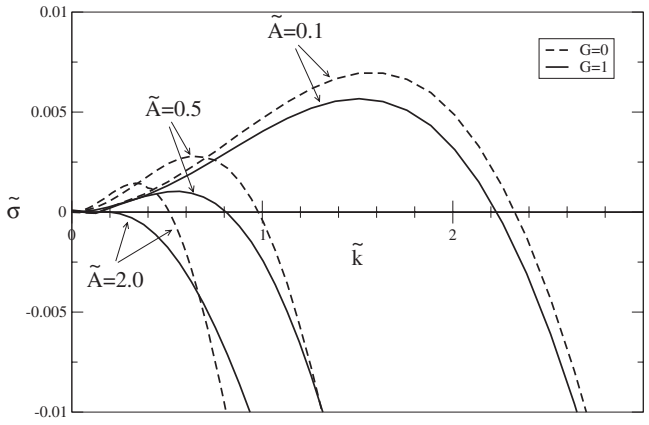

FIG. 15. Dispersion relations for the three rivulet cross sections, $\tilde{A}$, with ($G=1$) and without ($G=0$) gravity. The pressures for $\tilde{A}=0.1,0.5,2.0$ are $\tilde{p}=0.993,0.600,0.520$ for $G=1$, and $\tilde{p}=0.905,0.400,0.212$ for $G=0$. Here $\theta=30°$.

sectional areas. The Rayleigh–Plateau result, Eq. (26), is shown as dashed-dotted line [see also Fig. 5].

When gravity is included ($G=1$), Fig. 16 shows that much smaller values of k_c's result. Therefore, particularly for large $\tilde{A}$'s, gravitational effects are stabilizing and lead to substantially longer wavelength of instability. Figure 16 also shows the prediction of Ref. 13, calculated using Eqs. (27) and (28). Reasonably good agreement with our results suggest that for the rivulets considered here, vdW forces are not crucial in determining stability properties.

An explicit comparison of the results of the LSA including gravitational effects with physical experiments[31] is presented in Ref. 32. In that paper we show that the model with vdW and gravity compares favorably with experiments carried out with rivulets in millimeter range.

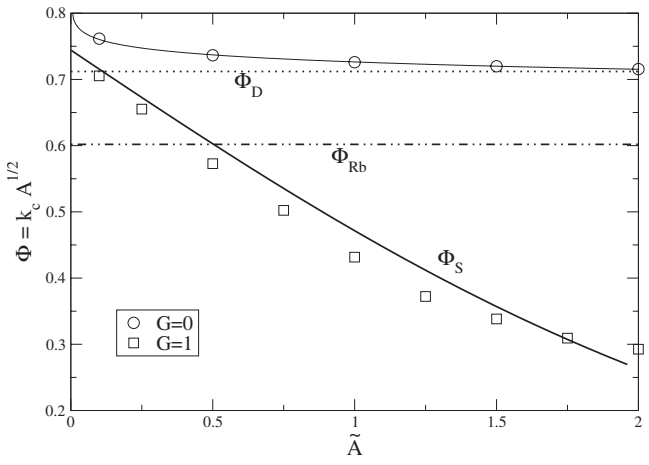

FIG. 16. Dimensionless combination Φ as a function of the cross section of the rivulet, $\tilde{A}$, as obtained from LSA with ($G=1$, squares) and without ($G=0$, circles and the thin solid line serving as a guide for the eye) gravity. Note that $\Phi=k_cA^{1/2}=\tilde{k}_c\tilde{A}^{1/2}$. The dotted line corresponds to the Φ given by Eq. (18), and the dashed-double dotted line to Rayleigh–Plateau result, Eq. (26). The thick solid line is the prediction of Ref. 13. Here, we use $\theta=30°$ and assume $\theta_0=\theta$.

V. NUMERICAL SIMULATIONS OF RIVULETS OF FINITE AND INFINITE LENGTH

In this section, we present fully nonlinear time-dependent simulations of rivulets, including both vdW forces and gravitational effects. First, we consider infinite-length rivulets and compare the results to the LSA carried out in Sec. IV. Then, we concentrate on finite-length rivulets and discuss the effect of this finite length on the instability development. To set this in perspective, we note that the analysis in Ref. 9 has shown that finite extent of a thin *film* can have a profound effect on the instability development. In the second part of this section we discuss whether a similar conclusion can be extended to the *rivulet* case.

The results in this section are obtained by solving the nonlinear equation (31). The details of the numerical procedure can be found in Ref. 33 and here we just give an outline. The calculations are carried out in a rectangular computational domain defined by $0\le\tilde{x}\le\tilde{X}$ and $0\le\tilde{y}\le\tilde{Y}$, divided into cells of size $\delta\tilde{x}\times\delta\tilde{y}$ (typically, we use $\delta\tilde{x}=\delta\tilde{y}=0.04$). Equation (31) is discretized in space using a central finite difference scheme, and a Crank–Nicolson method is used for the time evolution. We note that all the results that follow are fully converged, as verified by grid refinement. Due to symmetry of the considered problem, we simulate only one-quarter of a rivulet.

A. Rivulet of infinite length

We analyze here the evolution of the rivulet under two different types of perturbations, namely, infinitesimal disturbance, and localized finite amplitude disturbance, in analogy to the thin film problem.[9]

1. Infinitesimal perturbation

We take a numerical domain length, $\tilde{L}$, coincident with the wavelength of maximum growth, $\tilde{\lambda}_m=1.087$ obtained using LSA for $\tilde{p}=5$. We impose no-flow (or symmetry) conditions at the boundaries, which is equivalent to periodic boundary conditions for this infinite rivulet configuration. The free surface is perturbed at $\tilde{t}=0$ as prescribed by Eq. (36), where $\epsilon=10^{-3}$, and $\tilde{g}(\tilde{y})$ is given by the corresponding *varicose* eigenfunction [see Fig. 10(c)].

Figure 17 shows the time evolution of the free surface shape. The breakup (i.e., when the thickness reaches the value $h_{0,\min}$) is clearly observed in the middle of the domain. Figure 18 then shows the amplitude, $\tilde{\delta}$, of the perturbation at $(\tilde{x}=\tilde{L}/2,\ \tilde{y}=0)$, measured as the difference between the maximum thickness of the rivulet, $\tilde{h}_{\text{apex}}$, and the fluid thickness at that point. For early times, the growth of the perturbation follows an exponential law, as expected for a linear regime. This exponential law with growth rate σ_m is also shown in Fig. 18 (solid line).

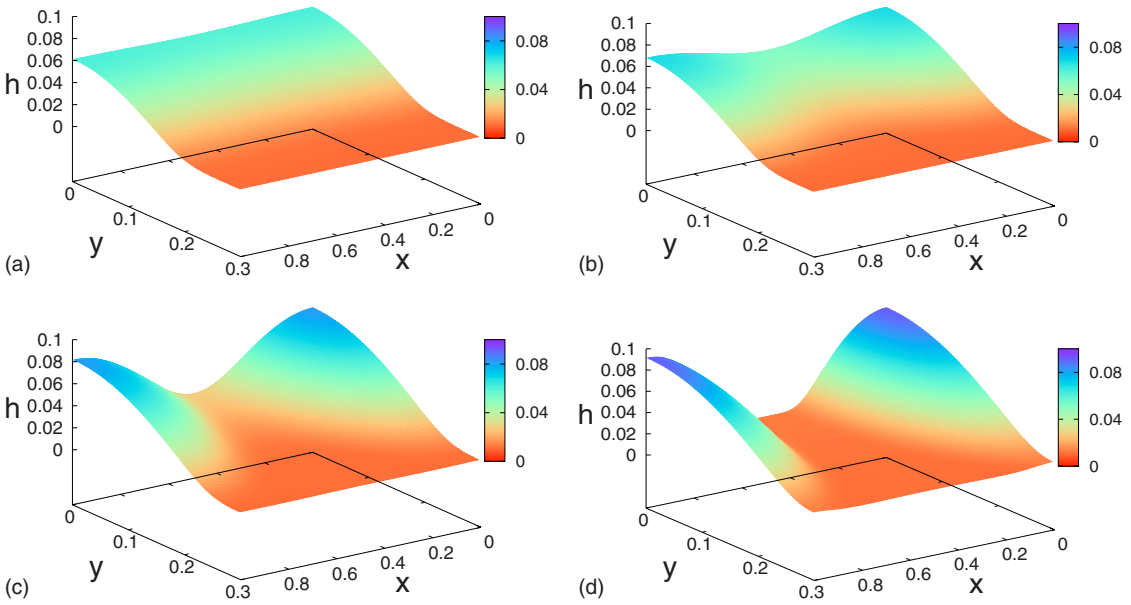

FIG. 17. (Color online) Evolution of a rivulet of length $\tilde{L}=1.087$ with $\tilde{p}=5$. We employ a perturbation with the wavelength $\tilde{\lambda}_m=\tilde{L}$.

2. Localized finite amplitude perturbation

Here we consider a long rivulet in the domain $0<\tilde{x}<\tilde{L}$ with $\tilde{L}\gg\tilde{\lambda}_m$ and impose a localized perturbation at $\tilde{x}=\tilde{x}_0$ for $\tilde{t}=0$. The initial condition is a perturbed steady state solution of the rivulet, $\tilde{h}_0(\tilde{y})$, of the form

$$\tilde{h}(\tilde{x},\tilde{y})=\tilde{h}_0(\tilde{y})\{1-\tilde{B}\exp[-(\tilde{x}-\tilde{x}_0)^2/\tilde{\Delta}^2]\}, \quad (42)$$

where $\tilde{B}$ and $\tilde{\Delta}$ are the depth and width of the perturbation, respectively. Here, we choose $\tilde{B}=0.2$ and $\tilde{\Delta}=0.4$, and obtain the evolution shown in Fig. 19. We see that the depression at $\tilde{x}_0=10$ increases with time, until a breakup occurs. Then, another depression appears, and the process repeats, so that eventually a sequence of drops is formed.

This mechanism of rivulet breakup has previously been studied in connection with the one dimensional (1D) rupture of flat thin films (see, e.g., Refs. 9 and 34 and the references therein). In the film breakup, there are two different types of instability: spinodal or nucleation instability. These regimes

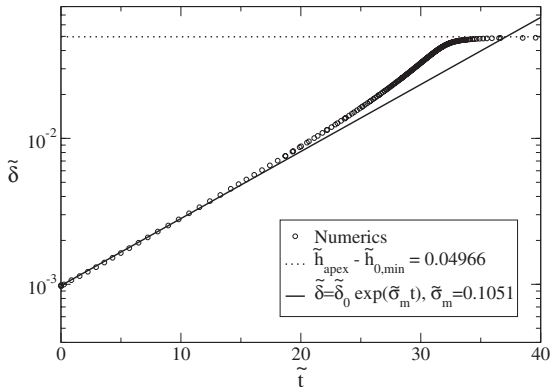

FIG. 18. Evolution of the amplitude, $\tilde{\delta}$, of the perturbation at $(\tilde{x}=\tilde{L}/2,\ \tilde{y}=0)$ with $\tilde{L}=\tilde{\lambda}_m=1.087$. The solid line shows LSA result. Here, $\theta=50°$ and $\tilde{p}=5$.

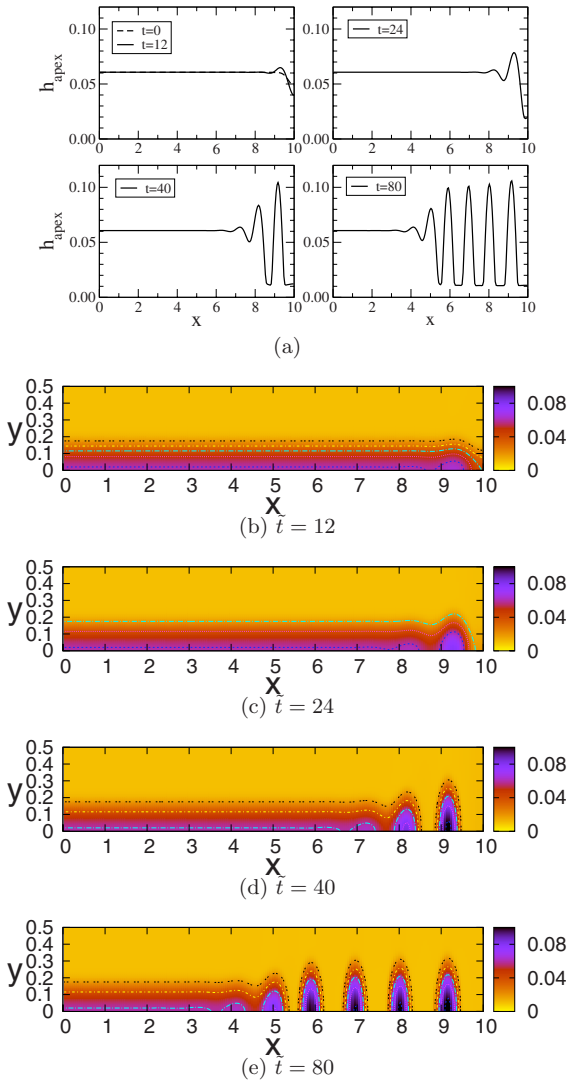

FIG. 19. (Color online) Evolution of an infinite rivulet with $\tilde{p}=5$ under a localized perturbation at $\tilde{x}_0=10$ given by Eq. (42). Part (a) shows $h_{apex}(x,t)$ profiles at a series of times, while parts (b)–(e) show two-dimensional (2D) contour plots of $h(x,y,t)$.

are determined by the film thickness, with nucleation being relevant for thinner films. The main difference between the final patterns formed by these two mechanisms is the distance, $\tilde{\ell}$, between consecutive 1D drops. In the spinodal regime, $\tilde{\ell}$ is given by the wavelength, $\tilde{\lambda}_m$, of maximum growth rate following from the LSA, while in the nucleation regime $\tilde{\ell}$ is not correlated with $\tilde{\lambda}_m$.

We have verified, at least numerically, that the nucleation mechanism relevant for thin films is not present in the rivulet case. This was done by carrying out a number of simulations such as the one shown in Fig. 19, where we have varied $\tilde{p}$ and $\tilde{h}_{0,\min}$. In all the cases studied ($\tilde{p}_c=0.845<\tilde{p}<6$), we find that the distance between the drops resulting from nonlinear evolution of a rivulet subject to finite size perturbation is very close to the one given by LSA, i.e.,

$$\tilde{\ell} \approx \tilde{\lambda}_m. \tag{43}$$

For example, for the case shown in Fig. 19, we find $\tilde{\ell} \approx 1.090$, which is very close to $\tilde{\lambda}_m \approx 1.087$. The point that the nucleation instability mechanism is not present in the rivulet case has been briefly pointed out in Ref. 21.

B. Rivulet of a finite length

Next, we consider the evolution of a rivulet of finite length. As in Ref. 9, we choose an initial condition given by a modulated steady solution of an infinite rivulet

$$\tilde{h}(\tilde{x},\tilde{y},0) = \tilde{h}_{0,\min} + H(x)[\tilde{h}_0(\tilde{y}) - \tilde{h}_{0,\min}], \tag{44}$$

where

$$H(x) = \frac{1}{\pi}[\arctan \tilde{q}(\tilde{x}-\tilde{x}_1) - \arctan \tilde{q}(\tilde{x}-\tilde{x}_2)], \tag{45}$$

and $\tilde{x}_1$, $\tilde{x}_2$ are the coordinates of the end points so that the fluid length is $\tilde{L}=\tilde{x}_2-\tilde{x}_1$. The $\tilde{x}$-length of the computational domain is $\tilde{X}=\tilde{L}/2+1$, allowing for the equilibrium film region ahead of the rivulet. The value of $\tilde{q}$ determines the width of the transition region between the unperturbed rivulet of thickness $\tilde{h}_{\text{apex}}$ and the equilibrium film region of thickness $\tilde{h}_{0,\min}$. We use a relatively large $\tilde{q}$ (typically, $\tilde{q}=100$) to obtain an initial condition resembling a step function connecting $\tilde{h}_0(\tilde{y})$ and $\tilde{h}_{0,\min}$ at the end points of the bulk. We have verified that varying $\tilde{q}$ (say, $50<\tilde{q}<500$) has only minor influence on the results that follow. Note that the initial condition, Eq. (44), is not a steady state solution of the problem, and thus, no perturbation is necessary to trigger the instability.

Figure 20 shows a typical evolution of a finite length rivulet for pressure $\tilde{p}=5$. We observe breakup process propagating from the rivulet end in a very similar manner as in Fig. 19, where we considered the effect of a finite size perturbation on an infinite rivulet. For the finite length rivulet shown in Fig. 20, we find that the average distance between the drops is $\tilde{\ell}' \approx 1.03$, very close to λ_m. Similar results are obtained for other values of $\tilde{p}$.

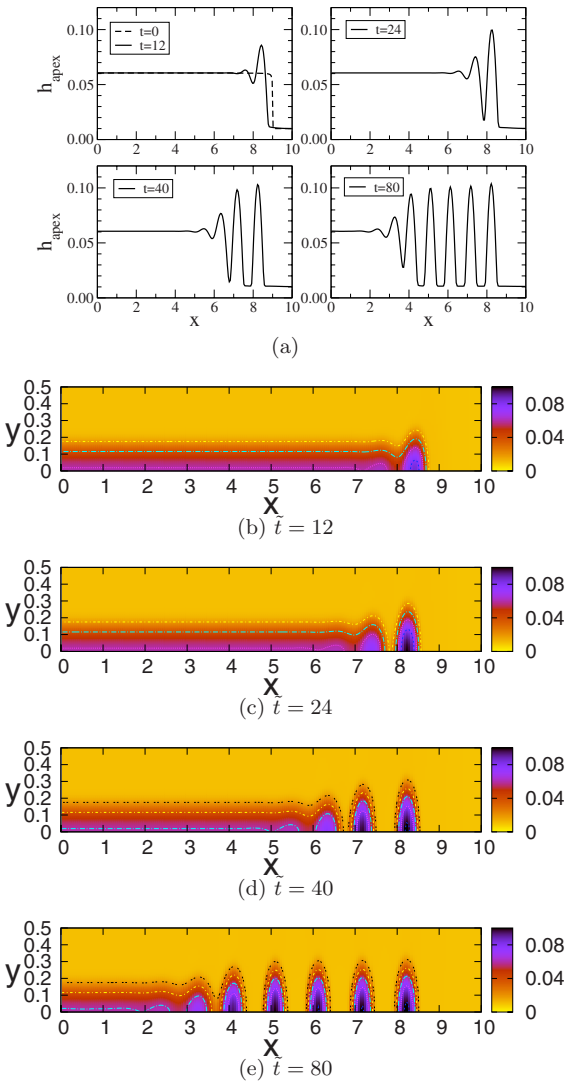

FIG. 20. (Color online) Evolution of a finite rivulet of length $\tilde{L}=18$ ($\tilde{x}_2=9$, $\tilde{x}_1=-9$) with $\tilde{p}=5$. Part (a) shows $h_{\text{apex}}(x,t)$ profiles at a series of times, while parts (b)–(e) show 2D contour plots of $h(x,y,t)$. The final pattern consists of drops separated by an average distance of $\tilde{\ell} \approx 1.03$.

The numerical simulations allow us to also study the time scales involved in the breakup process. The time needed for surface perturbations, such as those used in LSA [see Eq. (36)], to grow to a size comparable to the rivulet thickness is given by $\tilde{t}_s=-\ln \epsilon/\tilde{\sigma}_m$. For the example shown in Fig. 20, LSA gives $\tilde{\sigma}_m=0.114$, so, assuming an "infinitesimal" perturbation of amplitude $\epsilon=0.001$, we expect the breakup to occur around $\tilde{t}=80$. However, the breakup due to dewetting from the rivulet ends proceeds on a faster time scale than the growth of surface perturbations. Thus, surface perturbations do not have time to grow before the dewetting process generates the drops by breaking up the rivulet from the ends. This dominance of breakup driven by the dewetting from the ends was observed in recent experiments carried out with millimetric rivulets of polydimethylsiloxane on glass substrates.[31]

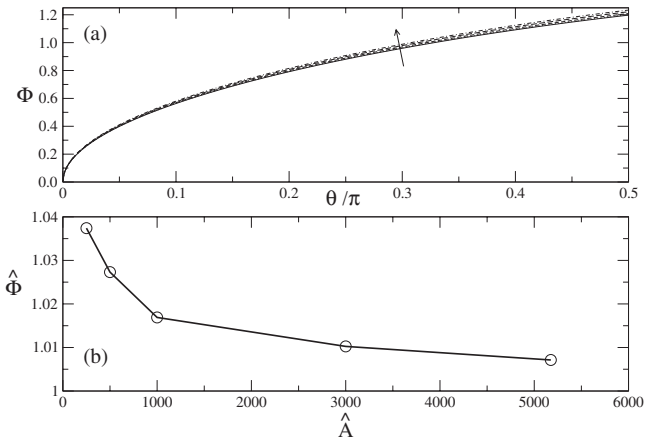

FIG. 21. (a) Critical wavenumber, k_c, as a function of θ for $\hat{A}=250$, 500, 1000, 3000, and 5000. The arrow indicates decreasing values of $\hat{A}$. (b) Dependence of $\hat{\Phi}=\hat{k}_c\hat{A}^{1/2}$ on $\hat{A}$.

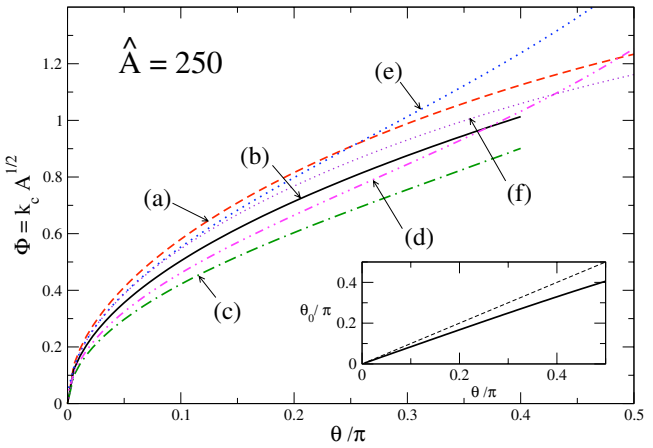

FIG. 22. (Color online) Comparison among three approaches for $\Phi=k_cA^{1/2}$ and $\hat{A}=250$: (a) LSA results, (red) dashed line, (b) Davis' theory (Ref. 12), Eq. (18), using $\theta_0(\theta)$, (black) solid line, (c) Rayleigh jet, Eq. (26), using $\theta_0(\theta)$, (green) dashed-dotted line, (d) Rayleigh jet, Eq. (26), using $\theta_0=\theta$ (magenta) dashed-double dotted line, (e) Brochard-Wyart and Redon (Ref. 7), Eq. (23), using $\theta_0=\theta$ (blue) dotted line, and (f) King *et al.* (Ref. 35) using $\theta_0=\theta$ (violet) dotted line (small dots). The relationship between $\theta_0(\theta)$ is shown in the inset, and the dashed line $\theta_0=\theta$ has been added for comparison.

VI. MICROSCOPIC RIVULETS

In this section, we focus on rivulets of nanometric thickness, where it is appropriate to consider a different scaling of the problem. On the first place, gravitational effects are not relevant, so we set $G=0$ here. On the nanometric scales, the equilibrium film thickness, h_*, used in the vdW model is comparable to the thickness of the main body of the rivulet, h_{apex}, and therefore, it makes sense to use h_* as an appropriate length scale for the out-of-plane direction,

$$h_s = h_*. \tag{46}$$

The horizontal scale is obtained by setting $K=1$, which yields

$$x_s^2 = Mh_*^2/(1-\cos\,\theta), \tag{47}$$

and, consequently, $t_s=(3\mu h_*/\gamma)[M/(1-\cos\,\theta)]^2$. An advantage of this approach is that the dependence of the solution on θ and h_* is prescribed since they are included in the scaling of the dimensionless variables. For instance, for cross-sectional area, we have that

$$\hat{A} = \frac{A}{h_*^2}\sqrt{\frac{1-\cos\,\theta}{M}}, \tag{48}$$

where the hat ˆ stands for dimensionless variables obtained when spatial scales x_s and h_s are defined by Eqs. (46) and (47).

Using this scaling, we carry out LSA analogously to Sec. III, but with $K=1$ and $G=0$. We focus again on the combination

$$\Phi = k_cA^{1/2} = \hat{k}_c\hat{A}^{1/2}\left(\frac{1-\cos\,\theta}{M}\right)^{1/4}. \tag{49}$$

Note that Φ and $\hat{\Phi}=\hat{k}_c\hat{A}^{1/2}$ are not equivalent now due to the different scalings used for horizontal and vertical directions. Thus, the left hand side depends on $\hat{A}$, not only due to the factor $\hat{A}^{1/2}$ but also through the value of $\hat{k}_c$ given by LSA for a fixed $\hat{A}$. Figure 21(a) shows Φ for several values of $\hat{A}$ with $0<\theta<\pi/2$. Figure 21(b) shows that $\hat{\Phi}\to 1$ as $\hat{A}\to\infty$. In this limit, we can write

$$\lambda_c \approx 2\pi A^{1/2}\left(\frac{M}{1-\cos\,\theta}\right)^{1/4}. \tag{50}$$

The dependence of λ_c on $A^{1/2}$ is in agreement with the experiments reported by Park *et al.*,[23] who studied rupture of polymer rivulets with width of 800–2500 nm on a silicon wafer. This scaling is also observed in recent experiments with laser-irradiated metal rivulets reported by Kondic *et al.*[11]

Figure 22 compares our LSA results [curve (a)] for the critical wavenumber with those discussed in Sec. II. In order to proceed, we must first calculate the relationship between θ (the contact angle in the definition of vdW forces) and θ_0 (the contact angle of the osculating circle), as done in Fig. 11 for a particular area. The result is shown in the inset of Fig. 22 for $\hat{A}=250$. In Fig. 22 we see that Ref. 12 predicts smaller k_c's compared to the LSA reported here; this difference increases for larger contact angles. We expect that this departure occurs due to the difference between θ and θ_0.

The Rayleigh–Plateau theory, given by Eq. (26) using $\theta_0(\theta)$ [curve (c)], also underestimates the LSA results. We note that if θ is used instead of θ_0 in that equation [curve (d)], a better agreement with LSA is obtained. This prediction is particularly good for $\theta=\pi/2$, as discussed recently for nanoscopic rivulets.[11] Finally, Fig. 22 shows that the result,[7] given by Eq. (23) [curve (e)], compares well with LSA for $\theta<\pi/4$, but overestimates k_c for larger angles.

Recently, we became aware of the work by King *et al.*,[35] where the authors derive approximate formulas for the eigenvalue problem via matched asymptotic expansions. Their result allows one to obtain Φ in a similar fashion as Eq. (49). Within their framework, we calculate the critical wavenum-

ber [see Eq. (4.24) in Ref. 35], and show it also in Fig. 22. We find that their result is in close agreement with the other results discussed so far.

VII. CONCLUSIONS

In this work, we have considered fully nonlinear evolution of fluid rivulets of finite and infinite length. In contrast to most of the previous works, we include liquid-solid interaction directly into the model and solve the resulting evolution equation. We then discuss in detail the limiting configurations for which our general results are consistent with the previously derived ones. In particular, we find that the circular cross section approach, pioneered by Davis,[12] emerges as a limiting case for rivulets characterized by large cross-sectional areas (small pressures) without gravity effects.

We carry out both linear stability analysis and fully nonlinear time-dependent simulations of the governing equation. We find that the results obtained using these two approaches are in full agreement, and therefore the distance between the drops that form during nonlinear evolution is closely related to the early evolution of perturbations as predicted by the LSA. In addition, we find that the wavelength of maximum growth rate predicted by the LSA also gives the distance between the drops resulting from nonlinear simulations where localized finite amplitude perturbations are imposed on infinite rivulets. This is in contrast to infinite and semi-infinite fluid films, where it is known that in the so-called nucleation regime, the distance between the drops may be unrelated to the one predicted by the LSA. For finite length rivulets, our simulations within a certain range of pressures suggest basically the same picture. Therefore, the ends of a rivulet act as if they were a localized and very large amplitude perturbation. For both finite and infinite-length rivulets, the distance between the drops is close to the one predicted by the LSA within the considered range of pressures.

The separation of results into macroscopic and microscopic rivulets allows two conceptually different views of the problem. In the macroscopic case, scaled with the capillary length, we are concerned with millimetric and submillimetric rivulets where gravitational effects are relevant. Here, vdW forces prevail only at the contact region and are negligible elsewhere. However, gravity qualitatively modifies the results by leading to much longer wavelengths, compared to the zero-gravity model. For microscopic (or nanometric) rivulets, gravity is irrelevant and vdW forces are essential all over the bulk. Thus, the appropriate scale is given by the equilibrium thickness of vdW forces. This allows us to obtain a simple relationship between the critical wavenumber, cross section and contact angle, see Eq. (49).

Finally, in this work we have compared explicitly the results of the theories which in one way or another include liquid-solid interaction, capillary and viscous forces, and the Rayleigh–Plateau theory for stability of a freestanding fluid jet. We find, perhaps surprisingly, reasonably good agreement between these approaches, therefore justifying the use of the Rayleigh–Plateau theory when only qualitative predictions are required. Even in this case, one has to be careful regarding the choice of a suitable Rayleigh–Plateau problem since different definitions may lead to significantly different results, particularly for large contact angles. If quantitative values are needed, appropriate physics, including liquid-solid interaction, needs to be included in the formulation.

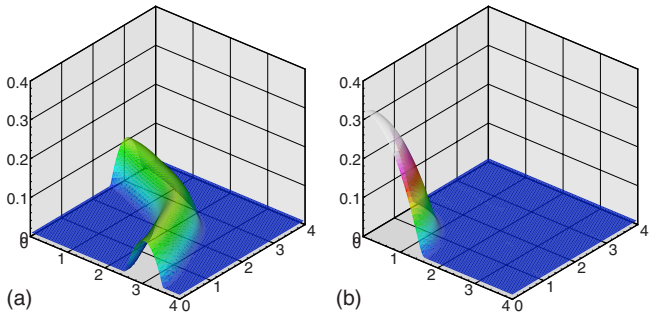

FIG. 23. (Color online) Evolution of a fluid ring of parabolic cross section with $\theta=30°$. The cross section is perturbed by a radial displacement with a wavenumber $n=8$. (a) $\hat{t}=0$; (b) $\hat{t}=200$.

An interesting extension of the present analysis is to consider a curved rivulet, closed in the form of a ring. This case has some similarity to an infinite rivulet with periodic boundary conditions, with the addition of azimuthal curvature. It is not obvious what type of evolution one should expect in this particular geometry. While it turns out that this problem is far from trivial and more work is required to understand its main features, here we show few preliminary results which serve to illustrate some features of this problem.

To begin with, we consider the evolution of a macroscopic ring under gravity with parabolic cross section,

$$\tilde{h}_0(\tilde{r}) = \tilde{h}_{\text{apex}}\left[1 - \left(\frac{\tilde{r}-\tilde{r}_0}{\tilde{r}_2-\tilde{r}_1}\right)^2\right], \quad \tilde{r}_1 \le \tilde{r} \le \tilde{r}_2,$$

with $\tilde{r}_0=3$, $\tilde{r}_1=2.5$, $\tilde{r}_2=3.5$, and $\tilde{h}_{\text{apex}}=0.1$. We perturb this initial condition with radial displacements in the form

$$\tilde{h}(\tilde{r}) = \tilde{h}_0[\tilde{r} - \delta\tilde{r}(\beta)],$$

where $\delta\tilde{r}=\tilde{C}\cos(n\beta)$, $\tilde{C}$ is a small amplitude, and β is the azimuthal angle.

Figure 23 shows the evolution for $\tilde{C}=10^{-3}$, $n=8$, and contact angle $\theta=30°$ (for simplicity we restrict the calculation to periodic solutions in one-quarter of the ring). Recalling the LSA carried out for a straight rivulet, one expects that a zig-zag type of the simulations used here is stable, and

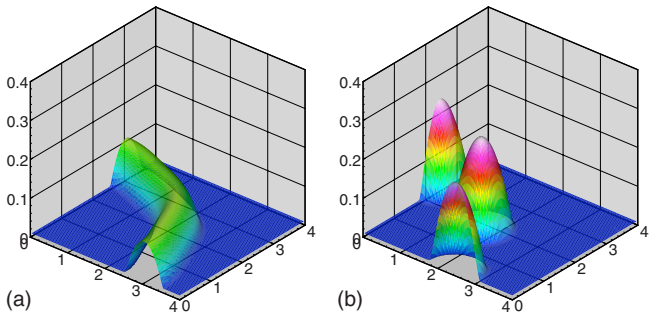

FIG. 24. (Color online) Same as Fig. 23 with $\theta=50°$. (a) $\hat{t}=0$; (b) $\hat{t}=200$.

therefore that the ring should converged to a single centrally placed drop. This is indeed what happens. However, when θ is increased to 50°, the evolution is quite different. Figure 24 shows that for this θ the ring breaks up into a drop and two halves in each quadrant, i.e., a total of eight drops for the complete ring. These results already indicate that the ring problem involves further challenges, and that one cannot simply extrapolate the results of the LSA carried out for a straight rivulet. This extension of the rivulet problem is presently under analytical and experimental studies.

ACKNOWLEDGMENTS

J.A.D. and A.G.G. acknowledge support from the Consejo Nacional de Investigaciones Científicas y Técnicas (CONICET, Argentina) and from the Agencia Nacional de Promoción de Científica y Tecnológica (ANPCyT, Argentina) under Grant No. PICT 2498/06. L.K. acknowledges support by NSF Grant No. DMS-0908158. We thank Steven Davis, Michael Miksis, and Burt Tilley for useful discussions.

[1] H. A. Stone, A. D. Stroock, and A. Ajdari, "Engineering flows in small devices," Annu. Rev. Fluid Mech. **36**, 381 (2004).
[2] H. A. Stone and S. Kim, "Microfluidics: Basic issues, applications, and challenges," AIChE J. **47**, 1250 (2001).
[3] K. J. Ruschak, "Coating flows," Annu. Rev. Fluid Mech. **17**, 65 (1985).
[4] H. S. Kheshgi, "The fate of thin liquid films after coating," in *Liquid Film Coating*, edited by S. F. Kistler and P. M. Schweizer (Chapman and Hall, London, 1997), p. 183.
[5] R. G. Larson and T. J. Regh, "Spin coating," in *Liquid Film Coating*, edited by S. F. Kistler and P. M. Scheizer (Chapman and Hall, London, 1997), p. 709.
[6] J. Becker, G. Grün, R. Seemann, H. Mantz, K. Jacobs, K. R. Mecke, and R. Blossey, "Complex dewetting scenarios captured by thin-film models," Nature Mater. **2**, 59 (2003).
[7] F. Brochard-Wyart and C. Redon, "Dynamics of liquid rim instabilities," Langmuir **8**, 2324 (1992).
[8] S. Herminghaus, K. Jacobs, K. Mecke, J. Bischof, A. Fery, M. Ibn-Elhaj, and S. Schlagowski, "Spinodal dewetting n liquid crystal and liquid metal films," Science **282**, 916 (1998).
[9] J. Diez and L. Kondic, "On the breakup of fluid films of finite and infinite extent," Phys. Fluids **19**, 072107 (2007).
[10] C. Favazza, R. Kalyanaraman, and R. Sureshkumar, "Robust nanopatterning by laser-induced dewetting of metal nanofilms," Nanotechnology **17**, 4229 (2006).
[11] L. Kondic, J. Diez, P. Rack, Y. Guan, and J. Fowlkes, "Nanoparticle assembly via the dewetting of patterned thin metal lines: Understanding the instability mechanism," Phys. Rev. E **79**, 026302 (2009).
[12] S. H. Davis, "Moving contact lines and rivulet instabilities. Part 1: The static rivulet," J. Fluid Mech. **98**, 225 (1980).
[13] K. Sekimoto, R. Oguma, and K. Kawasaki, "Morphological stability analysis of partial wetting," Ann. Phys. **176**, 359 (1987).
[14] G. W. Young and S. H. Davis, "Rivulet instabilities," J. Fluid Mech. **176**, 1 (1987).
[15] S. K. Wilson, B. R. Duffy, and A. B. Ross, "On the gravity-driven draining of a rivulet of viscoplastic material down a slowly varying substrate," Phys. Fluids **14**, 555 (2002).
[16] P. C. Duineveld, "The stability of ink-jet printing lines of liquid with zero receding contact angle on a homogeneous substrate," J. Fluid Mech. **477**, 175 (2003).
[17] D. Langbein, "The shape and stability of liquid menisci at solid edges," J. Fluid Mech. **213**, 251 (1990).
[18] R. V. Roy and L. W. Schwartz, "On the stability of liquid ridges," J. Fluid Mech. **391**, 293 (1999).
[19] L. Yang and G. M. Homsy, "Capillary instabilities of liquid films inside a wedge," Phys. Fluids **19**, 044101 (2007).
[20] S. Mechkov, M. Rauscher, and S. Dietrich, "Stability of liquid ridges on chemical micro- and nanostripes," Phys. Rev. E **77**, 061605 (2008).
[21] M. S. McCallum, M. J. Miksis, P. W. Voorhees, S. H. Davis, and H. Wong, "Capillary instabilities in solid thin films: Lines," J. Appl. Phys. **79**, 7604 (1996).
[22] H. Wong, M. J. Miksis, P. W. Voorhees, and S. H. Davis, "Universal pinch off of rods by capillarity-driven surface diffusion," Scr. Mater. **39**, 55 (1998).
[23] J. Park, K. Y. Suh, S. Seo, and H. H. Lee, "Anisotropic rupture of polymer strips driven by Rayleigh instability," J. Chem. Phys. **124**, 214710 (2006).
[24] The choice of the scaling and its dependence on the material parameters may be one of the reasons for the fact that the connection between the different results listed in the text has not been discussed in any detail until now.
[25] L. Yang and G. M. Homsy, "Steady three-dimensional thermocapillary flows and dryout inside a V-shaped wedge," Phys. Fluids **18**, 042107 (2006).
[26] L. A. Romero and F. G. Yost, "Flow in an open channel capillary," J. Fluid Mech. **322**, 109 (1996).
[27] C. Redon, F. Brochard-Wyart, and F. Rondelez, "Dynamics of dewetting," Phys. Rev. Lett. **66**, 715 (1991).
[28] K. B. Glasner and T. P. Witelski, "Coarsening dynamics of dewetting films," Phys. Rev. E **67**, 016302 (2003).
[29] A. L. Bertozzi, G. Grün, and T. P. Witelski, "Dewetting films: Bifurcations and concentrations," Nonlinearity **14**, 1569 (2001).
[30] K. B. Glasner and T. P. Witelski, "Collision versus collapse of droplets in coarsening of dewetting thin films," Physica D **209**, 80 (2005).
[31] A. G. González, J. Diez, R. Gratton, and J. Gomba, "Rupture of a fluid strip under partial wetting conditions," Europhys. Lett. **77**, 44001 (2007).
[32] J. A. Diez, A. G. González, and L. Kondic, "Stability of a finite-length rivulet under partial wetting conditions," J. Phys.: Conf. Ser. **166**, 012009 (2009).
[33] J. Diez and L. Kondic, "Computing three-dimensional thin film flows including contact lines," J. Comput. Phys. **183**, 274 (2002).
[34] U. Thiele, M. G. Velarde, K. Neuffer, and Y. Pomeau, "Film rupture in the diffuse interface model coupled to hydrodynamics," Phys. Rev. E **64**, 031602 (2001).
[35] J. R. King, A. Münch, and B. Wagner, "Linear stability of a ridge," Nonlinearity **19**, 2813 (2006).